Mechanistic Implications of Methylglyoxal Synthase Complexed with Phosphoglycolohydroxamic Acid As Observed by X-ray Crystallography and NMR Spectroscopy†

Gregory T. Marks,‡ Thomas K. Harris,§,|| Michael A. Massiah,§ Albert S. Mildvan,*,§ and David H. T. Harrison*,‡

Department of Biochemistry, Medical College of Wisconsin, 8701 Watertown Plank Road, Milwaukee, Wisconsin 53226-3548, and Department of Biological Chemistry, The Johns Hopkins University School of Medicine, 725 North Wolfe Street, Baltimore, Maryland 21205-2185

Received December 13, 2000; Revised Manuscript Received February 28, 2001

ABSTRACT: Methylglyoxal synthase (MGS) and triosephosphate isomerase (TIM) share neither sequence nor structural similarities, yet the reactions catalyzed by both enzymes are similar, in that both initially convert dihydroxyacetone phosphate to a *cis*-enediolic intermediate. This enediolic intermediate is formed from the abstraction of the *pro-S* C3 proton of DHAP by Asp-71 of MGS or the *pro-R* C3 proton of DHAP by Glu-165 of TIM. MGS then catalyzes the elimination of phosphate from this enediolic intermediate to form the enol of methylglyoxal, while TIM catalyzes proton donation to C2 to form D-glyceraldehyde phosphate. A competitive inhibitor of TIM, phosphoglycolohydroxamic acid (PGH) is found to be a tight binding competitive inhibitor of MGS with a K_i of 39 nM. PGH's high affinity for MGS may be due in part to a short, strong hydrogen bond (SSHB) from the NOH of PGH to the carboxylate of Asp-71. Evidence for this SSHB is found in X-ray, ^{1}H NMR, and fractionation factor data. The X-ray structure of the MGS homohexamer complexed with PGH at 2.0 Å resolution shows this distance to be 2.30−2.37 ± 0.24 Å. ^{1}H NMR shows a PGH-dependent 18.1 ppm signal that is consistent with a hydrogen bond length of 2.49 ± 0.02 Å. The D/H fractionation factor (ϕ = 0.43 ± 0.02) is consistent with a hydrogen bond length of 2.53 ± 0.01 Å. Further, ^{15}N NMR suggests a significant partial positive charge on the nitrogen atom of bound PGH, which could strengthen hydrogen bond donation to Asp-71. Both His-98 and His-19 are uncharged in the MGS−PGH complex on the basis of the chemical shifts of their Cδ and Cϵ protons. The crystal structure reveals that Asp-71, on the *re* face of PGH, and His-19, on the *si* face of PGH, both approach the NO group of the analogue, while His-98, in the plane of PGH, approaches the carbonyl oxygen of the analogue. The phosphate group of PGH accepts nine hydrogen bonds from seven residues and is tilted out of the imidate plane of PGH toward the *re* face. Asp-71 and phosphate are thus positioned to function as the base and leaving group, respectively, in a concerted suprafacial 1,4-elimination of phosphate from the enediolic intermediate in the second step of the MGS reaction. Combined, these data suggest that Asp-71 is the one base that initially abstracts the C3 *pro-S* proton from DHAP and subsequently the 3-OH proton from the enediolic intermediate. This mechanism is compared to an alternative TIM-like mechanism for MGS, and the relative merits of both mechanisms are discussed.

Understanding two enzymes that appear to be related by convergent evolution can be a powerful tool for elucidating the subtleties of catalysis. Methylglyoxal synthase (MGS,[1] EC 4.2.99.11) and triosephosphate isomerase (TIM) use the same initial chemical steps to form the enediol(ate) of dihydroxyacetone phosphate (DHAP) to catalyze faithfully the elimination of phosphate and the isomerization of the substrate, respectively. In both MGS and TIM, the first step of the reaction mechanism involves the stereospecific abstraction of the C3 proton of DHAP to form a common enediolic intermediate (*9, 10*). However, MGS abstracts the *pro-S* proton, whereas TIM abstracts the *pro-R* proton. MGS then catalyzes the 1,4-elimination of phosphate from the enediol(ate) to form the enol of methylglyoxal, as a product

† This research was supported by National Institutes of Health Grants DK 51697 to D.H.T.H. and DK 28616 to A.S.M. and a grant from the Juvenile Diabetes Foundation International to D.H.T.H. PDB Accession #1IK4. RCSB ID #RCSB013355.

* To whom correspondence should be addressed. D.H.T.H.: telephone, (414) 456-4432; fax, (414) 456-6510; e-mail, harrison@eeyore.biochem.mcw.edu. A.S.M.: telephone, (410) 955-2038; fax, (410) 955-5759; e-mail, mildvan@welchlink.welch.jhu.edu.

‡ Medical College of Wisconsin.

§ The Johns Hopkins School of Medicine.

|| Present address: Department of Biochemistry and Molecular Biology (R-629), University of Miami School of Medicine, 1011 NW 15th St., Miami, FL 33136.

[1] Abbreviations: DHAP, dihydroxyacetone phosphate; DMSO-d_6, perdeuterated dimethyl sulfoxide; GAP, glyceraldehyde 3-phosphate; HMQC, heteronuclear multiple-quantum coherence; ITC, isothermal titration calorimetry; MGS, methylglyoxal synthase; NOE, nuclear Overhauser effect; NOESY, nuclear Overhauser effect spectroscopy; PEG, polyethylene glycol; PGA, phosphoglycolate; PGH, phosphoglycolohydroxamic acid; P_i, inorganic phosphate; rmsd, root-mean-square deviation; *S*/*N*, signal-to-noise ratio; SSHB, short, strong hydrogen bond; SS NOESY, symmetrically shifted NOESY; TIM, triosephosphate isomerase; TPPI, time-proportional phase incrementation; Tris-d_{11}, perdeuterated tris(hydroxymethyl)aminomethane; TSP, 3-(trimethylsilyl)propionate-2,2,3,3-d_4.

10.1021/bi0028237 CCC: $20.00
Published on Web 05/10/2001

(eq 1).

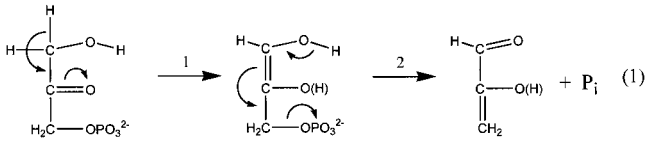

In contrast, TIM reprotonates the enediol(ate) intermediate at C2 to form glyceraldehyde 3-phosphate (GAP) (eq 2).

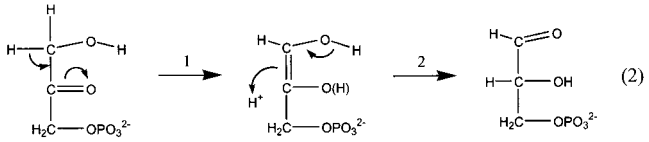

Both enzymes catalyze their respective reactions with remarkably similar kinetic constants: $k_{cat} = 220\ s^{-1}$, $K_m = 0.2$ mM, and $k_{cat}/K_m = 1.1 \times 10^6\ M^{-1}\ s^{-1}$ for MGS, and $k_{cat} = 600\ s^{-1}$, $K_m = 0.65$ mM, and $k_{cat}/K_m = 9.2 \times 10^5\ M^{-1}\ s^{-1}$ for TIM (*2*, *10*). Spectrophotometric evidence (I. A. Rose, personal communication) and the observation that the C3 position of methylglyoxal is protonated nonstereospecifically (*9*) strongly suggest that the enol aldehyde is the actual product of MGS. This product dissociates and ketonizes in solution to form methylglyoxal.

Methylglyoxal synthase catalyzes the first reaction in the methylglyoxal bypass of the Embden−Myerhoff glycolytic pathway (*11*, *12*). The physiological benefits conferred on bacteria by the methylglyoxal bypass (methylglyoxal synthase and the glyoxalase system) are not well understood. Methylglyoxal, the ultimate product of methylglyoxal synthase, is cytotoxic in millimolar quantities and has been shown to be mutagenic and to interfere with de novo protein and nucleic acid synthesis (*13*−*16*). The *S*-D-lactoylglutathione intermediate of the detoxifying glyoxalase system is also toxic in millimolar quantities and is known to interfere with the synthesis of intermediate filaments (*17*). Attempts to understand the benefits conferred by methylglyoxal synthase have focused on growth under nonideal conditions. Recent evidence suggests that the role for this microbial enzyme may be to facilitate the transition between conditions of starvation and abundance (*18*). Alternatively, methylglyoxal is converted by glyoxalases I and II to D-lactate, which is utilized in cell wall biosynthesis by some Gram-negative bacteria. Interest in methylglyoxal metabolism in man stems in part from the suggestion that methylglyoxal is implicated in diabetic complications (*19*). Further interest comes from the ability of the human glyoxalase system to clear 2-oxoaldehyde-based chemotherapeutic drugs (e.g., methylglyoxal bisguanylhydrazone) from tumors, rendering the treatment ineffective (*20*). Commercial interest in methylglyoxal metabolism derives from the potential use of methylglyoxal synthase in engineered microorganisms to produce the industrially important compound 1,2-propanediol (*21*).

The crystal structure of methylglyoxal synthase showed that the enzyme is a homohexamer of subunits that have a core fold of an α/β protein (*22*, *23*). The crystal structure of MGS complexed with the intermediate analogue phosphoglycolate (PGA) located the six active sites and showed them to contain Asp-71 and His-98 positioned to function as base and acid catalysts, respectively. Alignment of the structure of the MGS−PGA complex with that of the TIM−PGA complex, superimposing the carboxylate planes of PGA, revealed two mechanistically significant differences between the two enzymes. While the Nϵ2 atoms of the acid catalysts His-98 of MGS and His-95 of TIM overlapped, the base catalysts, Asp-71 of MGS and Glu-165 of TIM, approached opposite faces of the carboxylate of PGA. This approach is consistent with the different stereochemistry of proton abstraction in step 1 of the MGS and TIM reactions (eqs 1 and 2) (*9*). Further, the bridging phosphoryl oxygen of PGA is out of the plane of the carboxylate in MGS but in the carboxylate plane in TIM. The location of this bridging phosphoryl oxygen has been used to explain in part why MGS catalyzes an elimination reaction (in step 2 of eq 1), while TIM does not (*23*, *24*).

Phosphoglycolohydroxamic acid (PGH) is isostructural with the enediol of DHAP, where the C3 of DHAP has been replaced with N3. Hence, PGH is a closer analogue of the enediol(ate) intermediate of both the MGS- and TIM-catalyzed reactions (*25*). A complex of TIM and PGH has been studied by both X-ray crystallography (as a dimer) and ^{1}H NMR spectroscopy (*26*−*28*). The proton resonances from the NOH and NH groups of the bound PGH molecule have been measured and suggest distances to Glu-165 that are not significantly different from those measured by X-ray crystallography. Crystallographic evidence shows that the distances from the carboxylate of Glu-165 to the NOH and NH groups of PGH are 2.7−3.1 and 2.5−2.7 Å, respectively, with coordinate errors of ±0.3 Å suggested by a Luzzati plot. The higher-precision NMR data suggest that there is an SSHB (2.57 ± 0.05 Å) between Glu-165 and the NOH of PGH, while the hydrogen bond between Glu-165 and the NH group of PGH is considered normal.

Since the arrangement of the carboxylate and the imidazole ring on MGS is similar to that of TIM, it was hoped that both crystallographic and NMR spectroscopic measurements on the MGS−PGH complex would shed new light on the function of this SSHB. However, it is found that the mechanistic differences in the second halves of the reactions catalyzed by these two enzymes can be rationalized by the observed differences in the binding mode and affinity for PGH. The crystallographic, NMR spectroscopic, and kinetic data presented here and in prior work (*2*, *22*, *23*) suggest a dual role for Asp-71 in the mechanism of MGS; it abstracts a proton first from C3 and then from hydroxyl O3 of DHAP. A preliminary abstract of this work has been published (*29*).

EXPERIMENTAL PROCEDURES

Materials. Dihydroxyacetone phosphate bis(ethyl ketal) dimer $(DHAP)_2$, reduced glutathione, yeast glyoxalase I, and the tris(monocyclohexylammonium) salt of phosphoglycolate (PGA) were purchased from Sigma Chemical Co. (St. Louis, MO). Deuterium oxide (D_2O, 99.96 at. % D) and perdeuterated dimethyl sulfoxide (DMSO-d_6) were from Aldrich (Milwaukee, WI). Tris-d_{11} was from Isotec, Inc. (Miamisburg, OH). Unlabeled and ^{15}N-labeled phosphoglycolohydroxamic acid (PGH) (*28*) and MGS (*2*) were prepared as described. The pET-16b(+) bacterial expression vector was from Novagen (Madison, WI). DNA ligase and restriction enzymes were from Amersham Pharmacia Biotech (Piscataway, NJ). All solvents and reagents were of analytical or

reagent grade and were used without further purification unless otherwise indicated. All buffer solutions used in the NMR experiments were treated with Chelex-100 resin to remove trace paramagnetic metals and filtered through a 0.22 μm filter (Millipore) to remove Chelex particles before addition to NMR samples.

Wild-Type and Mutant Escherichia coli MGS Production. Recombinant *E. coli* MGS was expressed in pET16-mgswt or pET16-D71N transformed BL21(DE3) *E. coli* cells and purified as previously described (*2*). MGS was found to be ≥95% pure as determined by 14% SDS−PAGE (*30*) with Coomassie Blue staining and densitometric analysis as well as by its specific activity (200 units/mg) using the assay described below.

General NMR Methods. Unless otherwise stated, solution conditions for NMR studies were 0.6 mL of 0.7 mM MGS subunits in 20 mM Tris-d_{11}-HCl buffer (pH 6.0, 7.5, 9.0, or 11.0) with 10% (v/v) DMSO-d_6 and in the presence of 0−1.5 mM PGA or 0−1.5 mM PGH at −4.8 to 45 °C. DMSO-d_6 was added to the system to permit lowering of the temperature to <0 °C and for field/frequency locking. Its presence does not significantly affect the enzymatic activity. The NMR data were collected on a Varian Unity Plus 600 MHz spectrometer using a Varian 5 mm triple-resonance probe. Data were processed on a Silicon Graphics Indigo2 XZ Workstation using the FELIX 2.3 software package (Biosym Technologies, Inc.). Using the 1−3−3−1 pulse sequence (*31*) to avoid water excitation, one-dimensional ^{1}H NMR data sets were collected as described previously (*5*) with the following modifications. The delays between the pulses were adjusted for maximum excitation at 16.7 ppm (i.e., 12.0 ppm away from the carrier which is positioned at H_2O), and the acquisition parameters included a 2.5 s relaxation delay, a 512 ms acquisition time, and a 26 μs 90° pulse width. Multidimensional data sets were collected using the States−TPPI method (*32*) in all of the indirect dimensions, with relaxation delays of 2.0 s, and processed as described previously (*28*). The observed ^{1}H chemical shifts are determined with respect to the H_2O signal, which is 4.725 ppm downfield from external TSP at 30 °C and reported with respect to TSP. The ^{15}N chemical shifts are determined with respect to external $^{15}NH_4Cl$ (2.9 mM in 1 M HCl) at 20 °C, which is 24.93 ppm downfield from liquid ammonia (*33*), and are reported with respect to liquid ammonia.

^{1}H−^{15}N HMQC Spectra of ^{15}N-Labeled PGH Complexed with MGS. ^{1}H−^{15}N HMQC spectra were recorded using the 1−1 pulse sequence (*34*) modified by the addition of pulse-field gradients (*5*) in which the HMQC detection scheme was optimized to avoid water saturation. The data were obtained at 600 MHz with spectral widths of 1600 and 18 000 Hz in f_1 (^{15}N) and f_2 (^{1}H), respectively, and with 64 and 4608 complex points in the t_1 and t_2 dimensions, respectively. A total of 32 transients were acquired for each hypercomplex t_1 point with ^{1}H and ^{15}N carriers positioned at 4.72 and 175 ppm, respectively. The final data matrix was 256 × 256 real points for the f_1 (^{15}N) and f_2 (^{1}H) dimensions, respectively.

SS-NOESY Spectra of Free and PGH-Bound MGS. Two-dimensional NOESY spectra of free and PGH-bound MGS were acquired with 50 ms mixing times using the SS-NOESY pulse sequence (*5*, *35*) to avoid excitation of the water resonance by the detection pulse. The maximum excitation of the SS pulse (140 μs) was adjusted to be at 16.7 ppm, 7200 Hz from water. The sweep width was 20 000 Hz with 64 scans per FID and a recycle time of 2.0 s.

^{1}H NMR Titration of MGS with PGH. ^{1}H NMR titrations of wild-type MGS with PGH were performed by adding small portions (3−25 μL) of either a 5 or 50 mM stock solution of PGH (pH 7.5), prepared gravimetrically, to a 600 μL solution of 0.17 mM MGS (1.0 mM active sites). Since the complex of the reaction intermediate analogue, PGH, with MGS is in slow exchange on the chemical shift time scale (see the Results), the stoichiometry and dissociation constant for the complex could not be determined by following the changes in the ^{1}H chemical shift. Therefore, the stoichiometry (1.0 ± 0.1 PGH per monomer of MGS) was determined by plotting the increases in the relative peak intensities (I_{obs}) for the downfield resonances (δ = 18.1. 13.8, and 12.1 ppm) and the decrease in I_{obs} for the resonance at 13.3 ppm, which occur upon addition of PGH to free MGS, against the total concentration of PGH (L_{tot}), and an estimate of the dissociation constant (K_d) was determined from a fit of these data to eq 3.

$$I_{obs} = \frac{I_{max}[(K_d + L_{tot} + E_{tot}) - \sqrt{(K_d + L_{tot} + E_{tot})^2 - 4L_{tot}E_{tot}}]}{2E_{tot}} \quad (3)$$

Determination of Proton Exchange Rates. Limiting values of proton exchange rates with solvent for the downfield proton resonances in both free and PGH-bound wild-type and mutant MGS were determined from the temperature dependence of the ^{1}H resonance widths ($\Delta\upsilon_{1/2}$) over the range of −4.8 to 45 °C as described previously (*5*).

Determination of Fractionation Factors. Fractionation factors[2] (ϕ) for the downfield resonances in PGH-bound wild-type MGS were determined by integrating the corresponding ^{1}H NMR peaks at equilibrium in mixed H_2O/D_2O solutions (12, 27, 43, 58, 74, and 90% mole fraction H_2O) at 30 °C in the presence of 10% (v/v) DMSO-d_6 as described previously (*5*). Each sample contained 0.7 mM MGS and 1.5 mM PGH in 20 mM Tris-d_{11}-HCl (pH(D) 7.5) with 10% (v/v) DMSO-d_6 and was incubated at 4 °C for 24 h before NMR experiments were carried out. Accordingly, complete equilibration with D_2O was indicated by the unchanged intensities of the downfield protons after 72 h at 4 °C. The fractionation factors from the NMR-derived data were determined by nonlinear least-squares fits to eq 4:

$$I = \frac{I_{max}(X)}{\phi(1 - X) + X} \quad (4)$$

where I is the peak integral, X is the mole fraction H_2O, and I_{max} is the peak integral at 100% H_2O. The relative peak intensity was determined by normalizing peak integrals, I, to I_{max}.

PGH Inhibition Kinetics. The kinetic parameters k_{cat} and K_m were determined by fitting the data obtained from the Hopper and Cooper assay (*36*) to eq 5.

[2] The fractionation factor, ϕ, is defined as the equilibrium constant for replacement of a proton with a deuteron in a given system (*1*) (ϕ = [E−D][H_2O]/[E−H][D_2O]).

$$v = VA/(K_m + A) \quad (5)$$

where v is the velocity measured, V is the maximal velocity, A is the DHAP concentration, and K_m is the Michaelis−Menten constant. These parameters were compared to parameters determined previously (*2*).

The inhibition constant for the tight binding inhibitor PGH was determined from the relationship between enzyme concentration and velocity at a constant DHAP concentration (0.5 mM) using three concentrations of the inhibitor PGH, using the standard coupled assay conditions with 50 mM imidazole (pH 7.0) (*36*). These data were collected in duplicate and fit to eq 6 (*37*).

$$v = \frac{v_0}{2E_{tot}}[E_{tot} - I_{tot} - K_i + \sqrt{(E_{tot} - I_{tot} - K_i)^2 + 4E_{tot}K_i}] \quad (6)$$

where v_0 is equal to the velocity at zero inhibitor concentration, E_{tot} is the total enzyme concentration, I_{tot} is the total inhibitor concentration, and K_i is the inhibition constant.

To test the ability of PGH to activate MGS which had been allosterically inhibited by P_i, kinetic data were collected in duplicate, in the presence of 0.5 mM DHAP and 0.3 mM P_i over a wide range of PGH concentrations. These data were fit to eq 7 (eq VII-102 of ref *38*).

$$v = V\frac{\alpha(1 + \alpha + \theta)^{n-1}}{L + (1 + \alpha + \theta)^n} \quad (7)$$

where α is the ratio of the substrate concentration to its dissociation constant ($\alpha = [DHAP]/K_{d,DHAP}$), θ is the ratio of the inhibitor (PGH) concentration to its dissociation constant ($\theta = [I]/K_{d,I}$), L is the allosteric equilibrium constant, of the taut/relaxed forms of the free enzyme, and n is the Hill coefficient for ligand binding (*38*).

D71N Isothermal Titration Calorimetry. A dissociation constant for the binding of PGH to the D71N mutant of MGS in 50 mM imidazole buffer (pH 7.0) with 1 mM phosphate (storage buffer) was determined using isothermal titration calorimetry (ITC) according to the method of Wiseman et al. (*39*). All solutions were degassed prior to use. At 25 °C, 6.5 μL of a 0.48 mM PGH solution was injected every 240 s for 36 injections, into a 1.93 mL MicroCal ITC experimental cell that contained a solution that contained 60 μM MGS. Buffer into buffer, PGH into buffer, and buffer into MGS controls were all performed and subtracted as a baseline from the experimental data.

MGS−PGH Complex Crystallization and X-ray Data Collection. Orthogonal crystals of wild-type MGS complexed with the tight binding competitive inhibitor PGH were grown using the sitting drop method in 18% PEG 1500 and 100 mM sodium cacodylate at pH 6.5. Crystallization drops were made by mixing 4 μL of a 25 mg/mL MGS protein solution in 50 mM imidazole-HCl (pH 7.0), 1 mM KH_2PO_4, and 10 mM PGH with 4 μL of the crystallization solution. The crystal trays were incubated at room temperature for 1− 2 weeks. Image data were collected as previously described for MGS−PGA crystals (*40*). Reduced diffraction data from five different crystals were combined using the Program SCALEPACK from the HKL diffraction suite (*41*). Crystals of MGS complexed with PGH were found to be in space group $P2_12_12_1$ with the following cell dimensions: $a = 53.1$ Å, $b = 129.5$ Å, and $c = 178.5$ Å. Each asymmetric unit contained one MGS hexamer, resulting in a Matthew's coefficient V_m of 3.04 Å^3/Da. All of the data collection statistics are presented in Table 1.

Table 1: Crystal Parameters and Refinement Statistics

space group	$P2_12_12_1$
cell dimensions (Å)	$a = 53.1$, $b = 129.5$, $c = 178.5$
σ cutoff	0.0
resolution range (Å)	30.0−2.0 (2.03−2.00)[a]
total no. of reflections	467479
no. of unique reflections	84272
no. of reflections used in refinement	62475 (6217)
completeness (%)	81.6 (51.5)
R_{free} (%)	20.6 (30.0)
R factor (%)	16.9 (29.1)
no. of protein atoms	6971
no. of water atoms	400
no. of PGH atoms	60
Ramachandran most favored/additional (%)[b]	93.3/6.7
overall mean temperature factor (Å^2)	30.9
mean temperature factor for protein atoms (Å^2)	30.2
mean temperature factor for solvent atoms (Å^2)	42.9
rmsd from ideal[c]	
bond lengths (Å)	0.006
bond angles (deg)	1.2
dihedral angles (deg)	25.0
improper angles (deg)	0.66
coordinate error from Luzzati plot (Å)	0.24
	PDB Accession #1IK4

[a] Numbers in parentheses represent the last shell values. [b] Most favored and additional regions as defined by PROCHECK (*60*). [c] Root-mean-square deviations from Engh and Huber ideal values (*61*).

Refinement of the MGS−PGH Complex Structure. Prior to refinement, 7.5% of the data between 30.0 and 2.0 Å was set aside for the calculation of R_{free} (*42*) using the program DATAMAN (*43*). These data were selected in 15 discrete shells to take advantage of the effects of noncrystallographic symmetry (NCS) (*44*). Using the structure of the MGS−PGA complex (*40*) without the PGA molecule or the water molecules as a model for initial phases, the structure of the MGS−PGH complex was determined by isomorphous replacement using the program X-PLOR (*45*). The electron density maps clearly revealed the presence and position of the bound PGH in each active site. Prior to fitting the PGH molecule, the difference electron density map suggested two possible conformations for PGH. The structure was refined with the extended PGH confirmation as well as with both the extended and twisted confirmations at 50% occupancy. The structure with two confirmations suffered from a large increase in the R factor, suggesting that the only, or largely dominant, conformer is the one described here. Following the modeling of PGH and rigid body refinement, R was 20.4% and R_{free} was 24.2%. Following the addition of PGH and 400 water molecules, and several rounds of simulated annealing, positional refinement with noncrystallographic symmetry restraints, and eight rounds of manual rebuilding using the program O (*46*), the R factor and R_{free} converged to 16.9 and 20.6%, respectively. The Ramachandran plot shows that 93.3% of all residues fall within the most favored region. All of the refinement statistics are presented in Table 1. Luzzati plots were performed using the program XPLOR (*45*).

Structural Alignment. The program O (*46*) was used in a least-squares fitting algorithm to calculate a matrix that

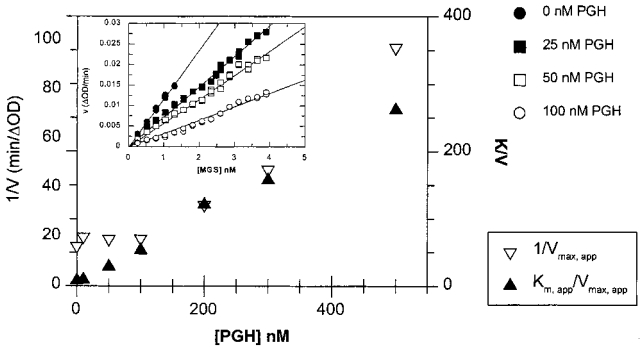

FIGURE 1: Inhibition of MGS by PGH. A plot of $1/V_{max}^{app}$ (▽) and $(K_m/V_{max})^{app}$ (▲) vs PGH concentration for a constant amount of wild-type enzyme (26 nM in subunits). The inset is a plot of velocity vs enzyme concentration at 0 (●), 25 (■), 50 (□), and 100 (○) nM PGH. The curves shown are generated by eq 6 with a K_i value of 39 nM for the tight binding competitive inhibitor PGH.

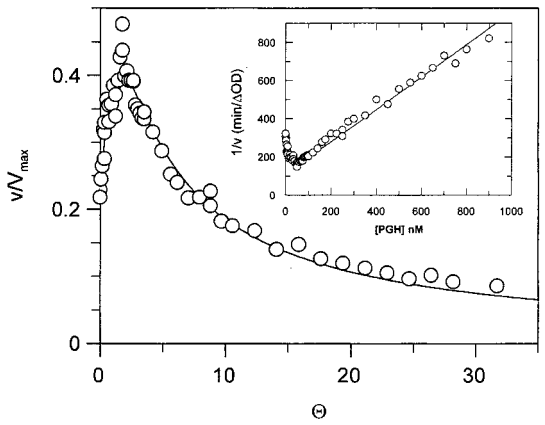

FIGURE 2: Activation of MGS by PGH in the presence of phosphate. A plot of v/V_{max} vs Θ for PGH according to eq 7 at 0.5 mM DHAP (substrate) and 0.3 mM P_i (allosteric inhibitor). Θ for each PGH concentration was determined after the K_i had been computed. The inset shows the same data shown as a Dixon Plot of $1/v$ vs PGH concentration.

overlays one structure upon another for structural comparisons. The program MOLMAN (*43*) was used to make a model of the mirror image of TIM (PDB entry 7TIM, molecule A) to superimpose the PGH ligands. The bound PGH ligand was used to manually position the mirror TIM molecule onto the active site of MGS using the program O.

RESULTS

Inhibition of Wild-Type Methylglyoxal Synthase by PGH. Freshly purified MGS was shown to have the same kinetic parameters (using eq 5) as those previously published (*2*). Inhibition kinetics of MGS with PGH did not strictly follow a competitive kinetic scheme as would be expected for an inhibitor that binds in the active site. Thus, the replots of $1/V$ and K/V versus PGH concentrations were nonlinear and showed neither a strictly competitive, noncompetitive, nor uncompetitive mechanism (Figure 1). An estimate of K_i of either 12 or 5 nM can be determined from the *x*-intercept of the K/V curve using PGH concentrations of <100 and 200 nM, respectively. The lack of linearity of these kinetics is explained in part by modeling PGH as a tight binding competitive inhibitor. PGH fits the four criteria for tight binding inhibitors as specified by Williams and Morrison (*47*), namely, that (i) the double-reciprocal plot appears to be noncompetitive, although the inhibitor is expected to be competitive, (ii) the plot of V versus I must be nonlinear, (iii) the inhibition is reversible, and (iv) the concentration of the inhibitor that causes observable inhibition (10 nM) must be approximately equal to the concentration of the enzyme (26 nM). Analysis of velocity versus the enzyme concentration at PGH concentrations of 0, 25, 50, and 100 nM, using eq 6, yields a competitive K_i of 39 ± 3 nM (Figure 1, inset).

It has been shown that a competitive inhibitor will activate an allosterically inhibited enzyme, like MGS in the presence of phosphate (*2*, *36*). Figure 2 shows a plot of v/V_{max} versus Θ according to eq 7, where the PGH concentration is varied and both DHAP and phosphate are held constant at 0.5 and 0.3 mM, respectively. Due to the large number of parameters, the data were fit to eq 7 assuming that the Hill coefficient is equal to the number of subunits and that the K_d of DHAP is equal to its K_m. On the basis of these assumptions, the K_i of PGH is found to be 36 ± 2 nM and the taut-to-relaxed ratio or allosteric equilibrium constant (L) is 3000 ± 300. This K_i is statistically identical to that determined from the fit of the kinetic data in Figure 1 to eq 6. The data depicted in Figure 2 can be transformed to give a more traditional Dixon plot (inset). This shows maximal activation by PGH of the enzyme, allosterically inhibited by phosphate, when the PGH concentration is 50 ± 10 nM, consistent with the K_i when PGH acts as an inhibitor.

Active Site from X-ray Structure. A PGH molecule is bound in the active site of all six subunits, with one solvent accessible water molecule (A) donating a hydrogen bond to the PGH O2 carbonyl oxygen (2.7 Å) and one buried water molecule (B) donating a hydrogen bond to the backbone carbonyl oxygen of Gly-66 (2.7 Å) and Oδ1 of Asp-101 (2.7 Å) (Figures 3 and 4). The distance from Asp-71 Oδ1 to water molecule B is 4.4 Å. The hydroxamic acid OH group appears to make an SSHB with Asp-71, with distances of 2.30−2.37 Å (average of 2.34 Å) for the six protomers. The Luzzati plot of the intensity data from the crystal suggests an estimated coordinate error of 0.24 Å. The existence of this SSHB has been confirmed by ^{1}H NMR, which estimates the bond distance to be 2.51 ± 0.02 Å (see below). In addition to donating an SSHB to Asp-71, the hydroxamic acid OH group potentially accepts a hydrogen bond from His-19 and the hydroxamic acid NH potentially donates a hydrogen bond to carboxylate Oδ2 of Asp-71. The nonburied water molecule (A) also potentially donates a hydrogen bond to the O2 carbonyl oxygen of the hydroxamic acid. The carbonyl oxygen of the hydroxamic acid may accept a hydrogen bond from His-98.

The phosphoryl moiety of the PGH is positioned above the N-terminus of the B helix, making a number of contacts identical to those in the formate/phosphate- and PGA-bound structures. It is held in a cage of nine hydrogen bonds from seven residues (Figures 3 and 4). These hydrogen bonds involve Nζ of Lys-23, Oγ of Thr-45, Thr-47, Thr-48, and Ser-65, the backbone amide nitrogen of Thr-47, Thr-48, and Gly-66, and Nη of Arg-150′ of the neighboring subunit. While the hydrogen bonds are the same as those found in the MGS−PGA complex, the distances vary enough to change the C1−C2 torsion angle. The average value of the angle for the O=C−C−OP torsion angle of the MGS-bound PGH molecule is $-38 \pm 5°$, while the equivalent torsion

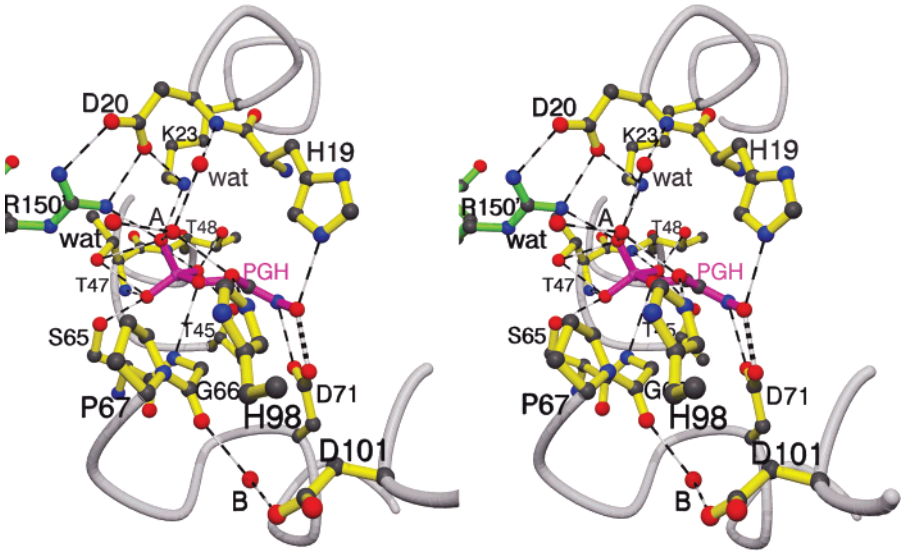

FIGURE 3: MGS−PGH complex. A stereodiagram of the active site of the MGS−PGH complex, including water molecules considered to be important to catalysis.

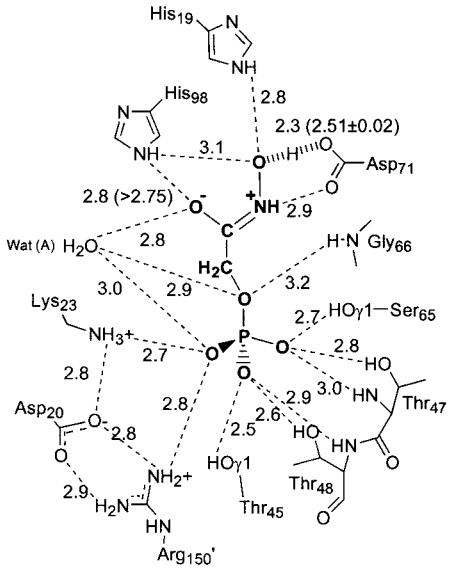

FIGURE 4: Schematic representation of the interactions between the active site residues and PGH. The distances (angstroms) shown are derived from an average of the distances found in the six individual protomers in the asymmetric unit in the crystal structure. The estimate of coordinate error from the Luzzati plot is 0.24 Å. Distances that are shown in parentheses are measurements from NMR spectroscopy.

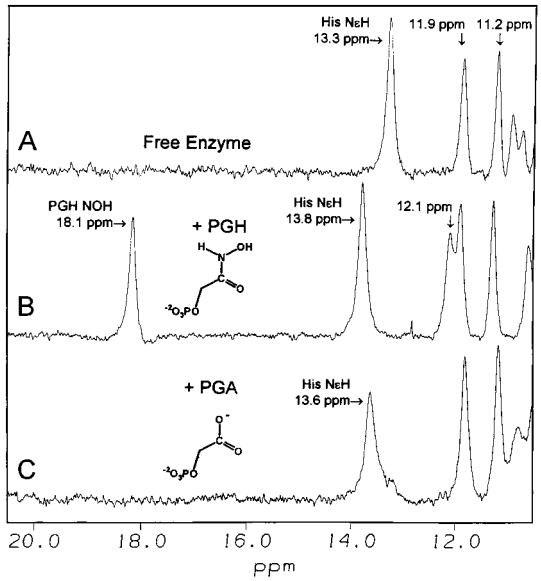

FIGURE 5: Low-field region of 600 MHz ^{1}H NMR spectra of 0.7 mM wild-type MGS subunits. (A) Free MGS. (B) Complex of MGS with 1.5 mM PGH. (C) Complex of MGS with 1.5 mM PGA. Other components that were present were 20 mM Tris-d_{11}-HCl (pH 7.5) and 10% (v/v) DMSO-d_6. T = 30 °C. Spectra were obtained as described in Experimental Procedures.

angles in the TIM−PGH and the MGS−PGA complexes are −11° and −57 ± 2°, respectively (*2*, *26*).

Assignment of Deshielded Proton Resonances of MGS. The low-field regions of the ^{1}H NMR spectra for free wild-type MGS and its complexes with the intermediate analogues PGH and PGA are shown in Figure 5. Free MGS exhibited well-resolved resonances at 13.3, 11.9, and 11.2 ppm and less well-resolved resonances near 10.9 and 10.7 ppm (Figure 5A). The resonances at 13.3, 11.9, and 11.2 ppm in free MGS are assigned to histidine NϵH protons on the basis of strong NOEs of similar intensities to pairs of aromatic resonances with chemical shifts in the range of histidine CδH and CϵH protons (Table 2). These low-field signals did not change in chemical shift or line width over the pH range of 6.5−11 (data not shown), suggesting the pK_a values of these histidines are <6. The resonance at 13.3 ppm exhibited an NOE to water protons, suggesting exposure to solvent (Table 2).

Titration of MGS with PGH resulted in a decrease in intensity of the 13.3 ppm signal with a corresponding increase in intensity of a resonance at 13.8 ppm (Figure 6), suggesting their assignment to the same residue, as well as the appearance of new signals at 18.1 and 12.1 ppm, and unresolved spectral changes between 10 and 11 ppm (Figure 5B). Analysis of the changes in the intensities of these resonances as a function of PGH concentration (Figure 6) reveals a stoichiometry of 1.0 ± 0.1 PGH molecules bound per monomer of this homohexameric enzyme. Because the K_d of PGH was much lower than the enzyme concentration required for the NMR titration (0.7 mM in subunits), its value was indeterminate by this method. From the NMR titration,

Table 2: NOEs between the Deshielded Proton Resonances and Active Site Protons Observed in Free MGS and in the MGS−PGH Complex

			NOEs to		
enzyme	resonance δ (ppm) (S/N)[a]	tentative assignment	deshielded resonance δ (ppm) (S/N)[a]	aromatic C−H resonance δ (ppm) (S/N)[a]	H_2O δ (ppm) (S/N)[a]
MGS	13.3 (34:1)	His-98 NϵH		6.99 (54:1), 8.24 (48:1)	4.73 (44:1)
	11.9 (36:1)	His-A NϵH	11.2 (3:1)	7.25 (20:1), 8.20 (34:1)	
	11.2 (54:1)	His-B NϵH	11.9 (3:1)	7.55 (40:1), 8.20 (45:1)	
MGS−PGH	18.1 (6:1)	PGH NOH	13.8 (2:1), 12.1 (2:1)	6.85 (5:1), 7.25 (3:1)	
	13.8 (9:1)	His-98 NϵH	18.1 (3:1), 12.1 (3:1)	6.85 (7:1), 7.55 (9:1)	
	12.1 (11:1)	His-19 NϵH	18.1 (5:1), 13.8 (5:1)	6.85 (8:1), 7.25 (12:1), 7.80 (9:1)	
	11.9 (12:1)	His-A NϵH		7.25 (9:1), 8.20 (8:1)	
	11.2 (13:1)	His-B NϵH		7.55 (9:1), 8.20 (8:1)	

[a] S/N ratio in the optimal slice with a mixing time of 50 ms at 30 °C.

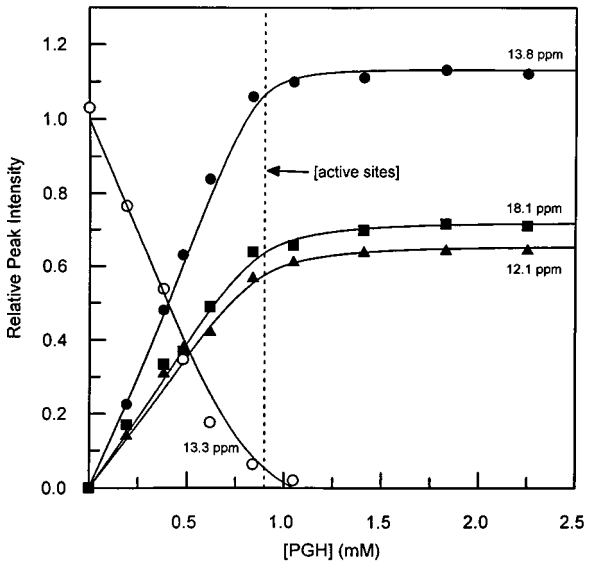

FIGURE 6: ^{1}H NMR titration of MGS (1.0 mM) with PGH. The decrease in the relative peak intensity of the His-98 NϵH proton in free MGS (δ = 13.3 ppm) (○) and increases in the relative peak intensities of the His-98 NϵH (δ = 13.8 ppm) (■), His-19 NϵH (δ = 12.1 ppm) (▲), and the PGH NOH protons in the MGS−PGH complex were followed in ^{1}H NMR spectra as the enzyme was titrated with PGH. The curves were generated by eq 3 using the following dissociation constants: $K_d = 6 \pm 15$ μM (○), $K_d = 2 \pm 2$ μM (●), $K_d = 14 \pm 9$ μM (■), and $K_d = 15 \pm 12$ μM (▲). The vertical dotted line represents the average concentration of enzyme active sites (0.9 mM) during the titration. For all curves, the binding stoichiometry is 1.0 per subunit.

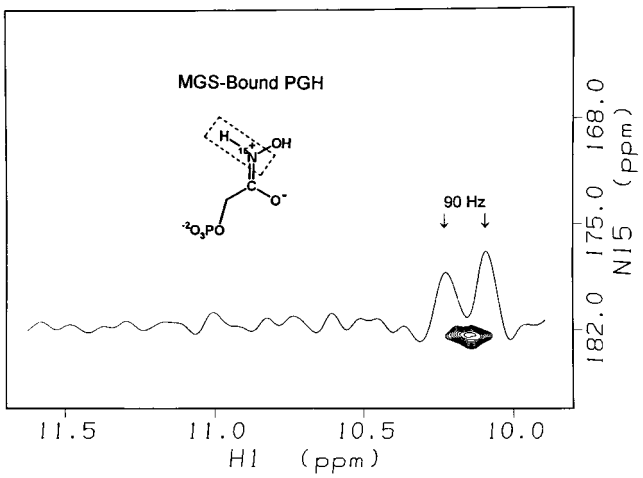

FIGURE 7: Two-dimensional ^{1}H−^{15}N HMQC spectrum of the [^{15}N]-PGH−MGS complex with ^{15}N decoupling. The sample contained 0.7 mM MGS subunits and 1.5 mM [^{15}N]PGH, and the other components and conditions are given in Figure 5. A one-dimensional slice through the cross-peak in the proton dimension of the ^{1}H−^{15}N HMQC spectrum of the [^{15}N]PGH−MGS complex obtained without ^{15}N decoupling is also shown and yields a $^1J_{N-H}$ value of 90 Hz. Spectra were obtained as described in Experimental Procedures.

one can conclude only that the K_d is sub-micromolar (Figure 6), consistent with the K_i value of 39 nM. In the MGS−PGH complex, the resonances at 13.8, 12.1, 11.9, and 11.2 ppm are assigned as histidine NϵH resonances on the basis of strong and equal NOEs to pairs of aromatic resonances (Table 2). These low-field signals in the spectrum of the MGS−PGH complex did not change in chemical shift or line width over the pH range of 6−11 (data not shown), again indicating pK_a values of <5.5.

The MGS−PGA complex exhibited well-resolved signals at 13.6, 11.8, and 11.2 ppm, and unresolved changes between 9.9 and 11 ppm (Figure 5C). Notably, unlike in the MGS−PGH complex, in the MGS−PGA complex, the resonance at 18.1 ppm is absent, suggesting that this signal comes from either the NOH or the NH proton of bound PGH. In the X-ray structure of the MGS−PGH complex, the two carboxyl oxygens of Asp-71 are within close hydrogen bonding distance of PGH N1 (2.85−2.95 ± 0.24 Å in the six subunits) and PGH O1 (2.30−2.37 ± 0.24 Å in the six subunits), suggesting that at least one of these proton resonances should be deshielded.

To clarify the assignments of the PGH NH and NOH proton resonances, two-dimensional ^{1}H−^{15}N HMQC spectroscopy was carried out using ^{15}N-labeled PGH bound to the enzyme. The two-dimensional NMR method correlates the ^{1}H and ^{15}N chemical shifts of directly bonded ^{1}H−^{15}N pairs by selecting for the large ^{1}H−^{15}N scalar coupling ($^1J_{N-H}$ ∼ 100 Hz) (*5*). The ^{1}H−^{15}N cross-peak in the two-dimensional HMQC spectrum of the MGS−[^{15}N]PGH complex at 30 °C with ^{15}N decoupling (Figure 7) gives ^{1}H and ^{15}N chemical shift values δ(^{1}H) of 10.2 ppm and δ(^{15}N) of 182 ppm. The chemical shift assignment of the NH proton of enzyme-bound PGH of 10.2 ppm indicates that the highly deshielded resonance at 18.1 ppm in the MGS−PGH complex (Figure 5B), which is absent in the MGS−PGA complex (Figure 5C), comes from the NOH proton. The large increase in the ^{15}N chemical shift of PGH from 168 ppm in the free ligand (*28*) to 182 ppm upon binding to MGS indicates a resonance form of enzyme-bound PGH with a significant amount of N3═C2 double bond character, and polarization of the C2 carbonyl group. Since a chemical shift of 182 ppm is also found in free PGH at pH 12 where the NO−H bond has ionized (pK_a = 9.5), the chemical shift of

Table 3: NMR Properties of Deshielded Proton Resonances in MGS Complexed with PGH at 30 °C[a]

δ (ppm)	tentative assignment	interaction (MGS···PGH)	ϕ	k_{ex}^{obsd} (s^{-1})	protection factor[b]	hydrogen bond length (Å) from δ	hydrogen bond length (Å) from ϕ	hydrogen bond length (Å) from X-ray[c]
18.1	PGH NOH	D71···HON	0.43 ± 0.02	<240	$>10^{1.2}$	2.49 ± 0.02	2.53 ± 0.01	2.30−2.37
13.8	His-98 NϵH	H98···O=C	1.18 ± 0.05	<280	$>10^{1.1}$	nd	>2.75	2.77−2.85
12.1	His-19 NϵH	H19···O−N	1.10 ± 0.07	<290	$>10^{1.1}$	nd	>2.75	2.93−3.10
11.9	His NϵH	nd	1.35 ± 0.04	<290	$>10^{1.1}$	nd	>2.75	nd
11.2	His NϵH	nd	1.11 ± 0.07	<185	$>10^{1.3}$	nd	>2.75	nd

[a] Chemical shift (δ), fractionation factor (ϕ), observed exchange rate with solvent (k_{ex}^{obsd}), and hydrogen bond lengths derived from δ, ϕ, and X-ray diffraction. [b] The protection factor is defined as the ratio of the observed proton exchange rate constant to the intrinsic proton exchange rate constant. The intrinsic exchange rate $k_{ex}^{intrinsic} = 3500\ s^{-1}$ for all of the exchangeable protons (*28*). [c] Range of values in the six subunits. The coordinate error is ± 0.24 Å.

182 ppm for enzyme-bound PGH indicates significant weakening of the NO−H bond.

The observation of $^1H-^{15}N$ coupling as indicated by the cross-peak in the TIM−[^{15}N]PGH complex provides evidence that the N−H bond in enzyme-bound PGH is intact. The $^1J_{N-H}$ value of enzyme-bound PGH (90 Hz) is lower than that of free PGH (102 Hz) (*28*), indicating slight weakening of the N−H bond. The NH proton chemical shift of 10.3 ppm in free PGH (*28*) shifts upfield to 10.2 ppm upon binding to MGS, consistent with a weak hydrogen bond, at best, as found by X-ray. While the signals at 11.9 and 11.2 ppm did not change in their shifts or NOEs upon PGH binding, the new histidine NϵH resonances at 13.8 and 12.1 ppm which appear in the complex, showed NOEs to the NOH resonance at 18.1 ppm, as well as to each other (Table 2), suggesting that these resonances are those of His-98 NϵH and His-19 NϵH. The appearance of the signal at 12.1 ppm in the MGS−PGH complex and its absence in the spectra of the MGS−PGA complex and of the free enzyme suggest its assignment to His-19 NϵH. In the X-ray structure of the PGH complex, His-19 interacts with the NOH group of PGH, but is solvent exposed both in the free enzyme and in the MGS−PGA complex. Hence, the resonance at 13.8 ppm in the MGS−PGH complex, which corresponds to the signal at 13.6 ppm in the MGS−PGA complex, is assigned to His-98 NϵH (Table 2). The chemical shifts of adjacent Cδ and Cϵ aromatic protons which show strong NOEs to His-98 NϵH and His-19 NϵH (Table 2) confirm that both His-98 and His-19 are uncharged in the MGS−PGH complex at pH 7.5. Hence, as suggested above, their pK_a values are <5.5.

Exchange Properties of the Deshielded Protons of MGS. The resonance widths of all of the downfield signals in free MGS, and in the MGS−PGH and MGS−PGA complexes, decreased with increasing temperature over the entire range that could be studied, from −4.8 to 45 °C, showing a purely dipolar contribution and no exchange contribution to their observed line widths ($1/T_{2obsd}$). Hence, the exchange rates of these resonances are much slower than ∼300 s^{-1} on the basis of their line widths at 30 °C (Table 3). The upper limit exchange rates of all the downfield resonances (<300 s^{-1}), compared to the exchange rate of an exposed neutral histidine NϵH proton (3500 s^{-1}) (*28*), indicate an at least 1 order of magnitude slowing of exchange or protection factor, consistent with participation of each of these protons in a hydrogen bond or hydrogen-bonded network.

Fractionation Factors of the Deshielded Protons of MGS. Fractionation factors (ϕ) for each of the downfield proton resonances in the MGS−PGH complex were determined by the intensities of the ^{1}H NMR signals in titrations in which the mole fractions of H_2O and D_2O were systematically varied. Figure 8 shows fits to eq 4 of the H_2O/D_2O titration data of the enzyme-bound PGH NOH proton signal at 18.1 ppm and the His-98 NϵH proton signal at 13.8 ppm which yield ϕ values of 0.43 ± 0.02 and 1.18 ± 0.05, respectively (Table 3). The ϕ values determined for the remaining deshielded histidine NϵH signals ranged from 1.10 to 1.35 (Table 3).

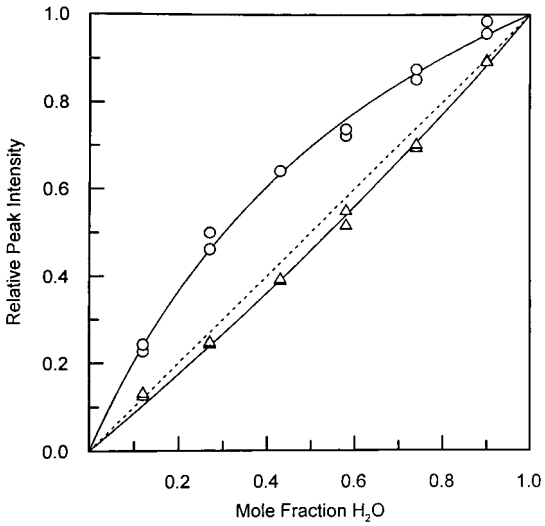

FIGURE 8: Determination of the fractionation factors of downfield proton resonances in the MGS−PGH complex. Plot of the relative peak intensity of the PGH NOH proton signal (δ = 18.1 ppm) (○) and the histidine NϵH proton signal (δ = 13.8 ppm) (△) in the MGS−PGH complex as a function of the mole fraction H_2O in the aqueous solution. Components and conditions are otherwise as given in the legend of Figure 5. The curves are described by eq 4 using a ϕ of 0.43 ± 0.02 (○) and a ϕ of 1.18 ± 0.05 (△); the dashed line is drawn for a ϕ of 1.

Effects of the D71N Mutation on the Deshielded Proton Resonances of MGS. The D71N mutation which resulted in an at least 2500-fold decrease in k_{cat}[3] yielded a protein spectrum which showed the disappearance of the His NϵH resonance at 13.3 ppm assigned to His-98 (Figure 9A), presumably due to exchange broadening. This disappearance suggests a hydrogen bond between Asp-71 and His-98 in the free wild-type enzyme. Such a hydrogen bond is found in the active site of free triosephosphate isomerase between Glu-165 and His-95 (*24*). The addition of a 3-fold excess of PGH did not alter the signals at 11.9 and 11.3 ppm but induced the appearance of four very weak deshielded

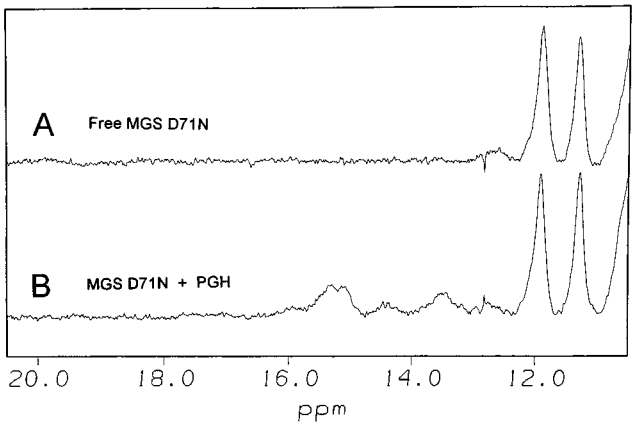

FIGURE 9: Low-field region of 600 MHz ^{1}H NMR spectra of 0.7 mM mutant MGS subunits. (A) Free D71N mutant MGS. (B) Complex of D71N mutant MGS with 1.5 mM PGH. Other components that were present were 20 mM Tris-d_{11}-HCl (pH 7.5) and 10% (v/v) DMSO-d_6. T = 30 °C. Spectra were obtained as described in Experimental Procedures.

resonances between 15.3 and 13.5 ppm. Importantly, no signal appeared at 18.1 ppm (Figure 9B). The low intensities of the signals between 15.3 and 13.5 ppm may well reflect heterogeneity among the six active sites. These weak signals could have resulted from upfield shifts of the 18.1 ppm resonance due to weaker hydrogen bonding from PGH NOH to Asn-71. Additionally, some of these signals may reflect histidine NH resonances but were too weak for this assignment to be confirmed by NOEs to carbon-bound protons.

Dissociation Constant for PGH Bound to the D71N Mutant of Methylglyoxal Synthase. Isothermal titration microcalorimetry measures the bulk properties of a macromolecular solution without yielding a significant signal due to contamination by small quantities of undesired proteins (*39*). The results from analysis of the binding curve give a dissociation constant (K_d) of 3.9 ± 1.1 μM, a binding enthalpy of −2.7 ± 0.3 kcal/mol, and a number of sites of 0.42 ± 0.03 per monomer. The presence of 1 mM phosphate during the titration was required to stabilize the enzyme. In the absence of phosphate, this enzyme rapidly becomes inactive. The low binding stoichiometry of PGH may have resulted from partial inactivation of this mutant or from negative cooperativity among the binding sites. The dissociation constant should be considered an upper limit because of possible competition with phosphate. Further evidence for instability of the D71N mutant enzyme is found in the ^{1}H NMR spectra that show a lower than expected signal-to-noise ratio for the deshielded proton resonances (Figure 9). Importantly, the measured inhibition constant (K_i) of PGH for this mutant enzyme is identical to that of the wild type and thus implies the presence of 1 in ~10^4 molecules of the wild-type enzyme in this and previous preparations of the D71N variant. Thus, the previously determined catalytic constant (k_{cat}, decreased by $10^{3.4}$-fold vs that of the wild type) must be considered an upper limit on the activity of the D71N variant, which could be totally inactive.[3]

Overall Structure of the MGS−PGH Complex. The overall structure of the MGS−PGH complex is virtually unchanged from either the MGS−PGA or MGS−formate/phosphate structures. The structure remains an α/β protein with an additional N-terminal β-strand that is antiparallel to an additional C-terminal β-strand that leads into a C-terminal α-helix. The overall least-squares fit of the Cα atoms of the phosphate/formate-bound subunit to each PGH bound subunit gives an rmsd of 0.21 Å, while the least-squares fit of the Cα atoms of each PGA bound subunit to the corresponding PGH bound subunit gives an rmsd of 0.10 Å.

Comparison of the PGH and PGA Complexes of MGS. There are numerous small changes in the active site, suggesting that the protein in the MGS−PGH complex is closing in on its inhibitor relative to the MGS−PGA complex (Figure 10). Overall, the active site appears to be quite rigid, with the exception of Asp-71 Oδ1 which changes position by only 0.4 Å. PGH and PGA in these complexes are bound within 0.2 Å of each other. However, there are some differences that lead to the formation of hydrogen bonds. The torsion angles of PGH in the MGS−PGH complex are quite different from the analogous torsion angles of PGA in the MGS−PGA complex such that there is only a 0.3 Å shorter distance from a nonbridging phosphoryl oxygen to Nη2 of Arg-150′ from the adjoining subunit. More strikingly, the bridging phosphoryl oxygen of PGH is located 0.7 Å from that position in PGA.

Comparison of the MGS−PGH and TIM−PGH Complexes. The mirror image of the TIM−PGH X-ray structure was aligned so that the hydroxamic acid moiety overlapped with the hydroxamic acid moiety of the MGS−PGH complex (Figure 11). Once these two structures were aligned, the carboxylate oxygens of Asp-71 (on MGS) had moved 1.1 and 1.8 Å from the C2 position of PGH relative to the positions of the corresponding carboxylate oxygens of Glu-165 (on TIM). Thus, the average hydrogen bond distances to the nearest carboxylate oxygen acceptor from the NOH and NH donors of the hydroxamic acid are 2.3 and 2.8 Å on MGS and 2.9 and 2.6 Å on TIM, respectively. However, the more precise and accurate carboxylate to NOH hydrogen bond lengths determined by ^{1}H NMR are 2.51 ± 0.02 and 2.57 ± 0.05 Å for the MGS−PGH and TIM−PGH complexes, respectively [Table 3 (*28*)].[4] The most obvious difference is within the PGH molecule itself. The O=C−C−OP torsion angle changes from −11° in the TIM−PGH

[3] The kinetic and calorimetric studies on the D71N mutant enzyme show the presence of trace amounts of the wild-type enzyme in this and other preparations of the variant (see the Results). Published measurements of the k_{cat} and K_m of D71N must be regarded as incorrect, although the published value of k_{cat} (reduced by $10^{3.4}$-fold) may be set as an upper limit on the true value of the k_{cat} of D71N (*2*), which may be totally inactive.

[4] The errors in interatomic distances determined by protein X-ray crystallography are generally 0.1−0.3 times the atomic resolution (*3*−*5*). In addition to being more precise, hydrogen bond lengths determined by δ and ϕ are highly accurate as indicated by measurements of the O···H···O distance in the small molecule sodium 4,5-dihydroxynaphthalene-2,7-disulfonate where the δ of 17.7 ppm and the ϕ of 0.56 ± 0.04 yield distances of 2.50 ± 0.02 and 2.57 ± 0.01 Å, respectively, with an average value of 2.54 ± 0.03 Å. These distances agree with the average ± standard deviation value of 2.55 ± 0.06 Å obtained from 22 high-resolution small molecule X-ray structures of dihydroxynaphthalene derivatives in the Cambridge Data Bank. Similarly, the histidinium−aspartate N−H···O distance in the catalytic triad of subtilisin is 2.63 ± 0.04 Å from the proton chemical shift of 17.4 ppm, using a correlation for imidazolium−carboxylate interactions from solid-state NMR and small molecule X-ray crystallography (*6*, *7*), and 2.56 ± 0.01 Å from its ϕ value of 0.53 ± 0.02. These distances, and their average (2.60 ± 0.04 Å), agree with the value of 2.62 ± 0.08 Å obtained from an unusually high-resolution X-ray structure (0.78 Å) of subtilisin (*8*).

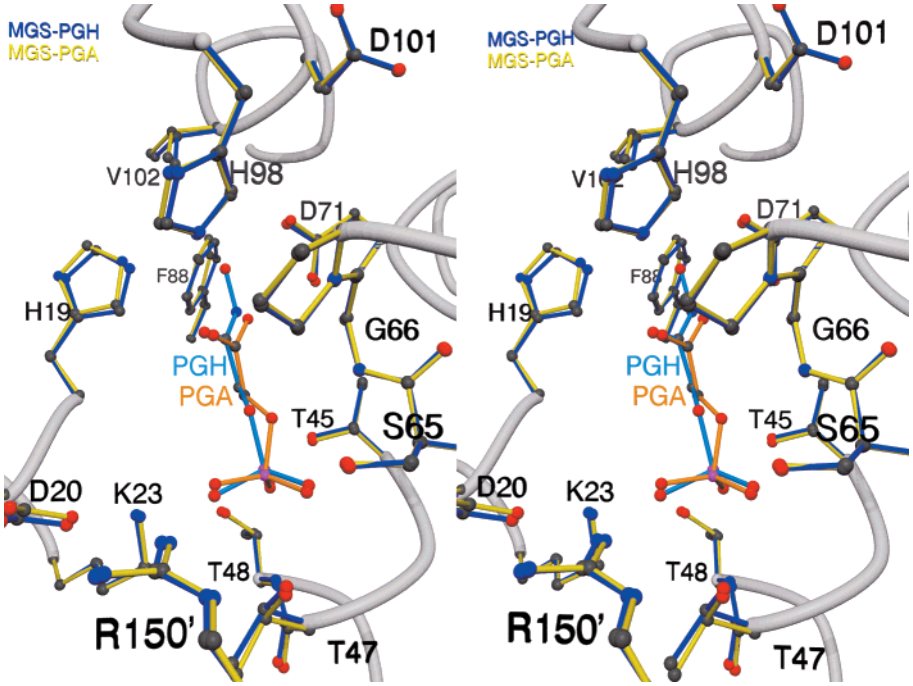

FIGURE 10: MGS−PGH complex compared to the MGS−PGA complex. A stereodiagram of the superposition of the MGS−PGA (yellow and orange) and MGS−PGH (dark blue and light blue) active site structures. The rmsd of the Cα atoms between these structures is 0.1 Å. However, there are significant differences found at the position of Asp-71 in MGS and the bridging phosphate oxygen of the inhibitors themselves.

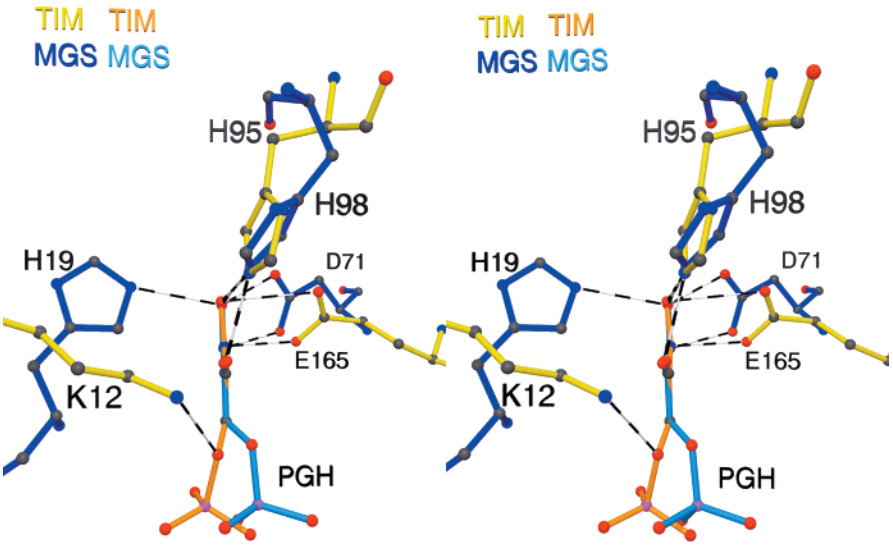

FIGURE 11: MGS compared to TIM. A stereodiagram of the superposition of the MGS−PGH (dark blue and light blue) and TIM−PGH (yellow and orange) complexes. Note that while the distances from the carboxylates of Asp-71 (of MGS) and Glu-165 (of TIM) to the hydroxamic acid are similar, the angle of attack is not. Additionally, note that the χ_1 torsion angle of His-95 of TIM enables movement of an NϵH proton between the oxygens in the enediolic plane, while the χ_1 angle of His-98 of MGS only enables movement of the imidazole ring across of the plane of the PGH molecule.

complex to −38° in the MGS−PGH complex. Although this difference in the torsion angles for the PGH complexes is not as great as in the PGA complexes, it does indicate an active participation by MGS in the control of this torsion angle to promote the elimination of phosphate.

DISCUSSION

The crystallographic and NMR studies together provide detailed information about the structure of the MGS−PGH complex, which is diagrammed in Figure 4. The NOH proton of enzyme-bound PGH with a chemical shift of 18.1 ppm is 9.4 ppm deshielded from that of PGH in solution (*28*). This extensive deshielding, as well as the low fractionation factor (ϕ) of 0.43, and the $>10^{1.2}$-fold protection factor against proton exchange with solvent meet the NMR criteria set forth for a short, strong, or low-barrier hydrogen bond (*5*). From the chemical shift, using a tight correlation from solid-state NMR and small molecule X-ray crystallography for O−H···O hydrogen bonds (*5*, *48*), we calculate a hydrogen bond length of 2.49 ± 0.02 Å between the carboxyl oxygen of Asp-71 and O1 of enzyme-bound PGH, taking into account the errors in chemical shift and in the correlation (Table 3). An independent measurement of this hydrogen bond length can be obtained from the fractionation factor. Using quartic

potential functions, Kreevoy and Liang (*49*) have computed ϕ values of hydrogen bonds as a function of distance between the proton wells, and these computations have been used to determine hydrogen bond lengths from measured ϕ values of ≤ 1.0 as described previously (*3*, *5*). The ϕ value of the NOH proton (0.43 ± 0.02) yields a hydrogen bond length of 2.53 ± 0.01 Å, taking into account the error in ϕ, which agrees with the hydrogen bond length of 2.49 ± 0.02 Å derived from its proton chemical shift (Table 3). These two independent NMR measurements overlap with the distances observed in the X-ray structure of $2.30-2.37 \pm 0.24$ Å (in the six subunits) but provide a more precise and accurate determination of this hydrogen bond length.[4] A D71−PGH hydrogen bond length of 2.30−2.37 Å would indicate extremely short hydrogen bond lengths which have been observed only in the gas phase for very strong, single-well hydrogen bonds such as F···H$^+$···F and O$^-$H···H$^+$···$^-$OH (*50*). For ϕ values >1.0, which may result from restricted bending motions which increase vibration frequencies (*51*, *52*), no precise distance dependence relationship has been calculated. In such cases, the simplest assumption is that such protons are in normal, weak hydrogen bonds with distances greater than the corresponding hydrogen bond length in water, the best estimate of which is that measured in ice (2.75 Å) (Table 3) (*53*). For the hydrogen bond from His-98 Nϵ2 to the carbonyl oxygen of PGH, where the fractionation factor is 1.18, the X-ray structure shows this hydrogen bond length to be $2.77-2.85 \pm 0.24$ Å in the six subunits.

The predominant imidate resonance form of PGH is shown in Figure 4, in accord with the 14 ppm deshielding of the ^{15}N signal of PGH on binding to MGS, and the N−H proton is shown based on the $^1J(^{15}\text{N}-\text{H})$ of 90 Hz (Figure 7). In both the TIM−PGH and MGS−PGH complexes, the N−H bond of PGH is largely intact. The PGH NOH hydrogen bond is slightly shorter and stronger on MGS than on TIM based on its chemical shift of 18.1 ppm in comparison with 14.9 ppm found on TIM (*28*). Conversely, the hydrogen bond to the C2 oxygen of PGH from a histidine NϵH is longer and weaker on MGS than on TIM. Despite this difference, there is more imidate polarization of PGH on MGS than on TIM, as indicated by the 14 and 6 ppm deshieldings of PGH N1 on MGS and TIM, respectively. The increased level of imidate polarization on MGS may result from the stronger PGH NOH hydrogen bond and resulting greater negative charge on the NOH oxygen.

Mechanistic Implications. A comparison of the k_{cat} of MGS (220 s^{-1}) (*2*) with the first-order rate constant for the uncatalyzed elimination (1.4×10^{-5} s^{-1}) (*54*, *55*) yields a rate acceleration or catalytic power of $10^{7.2}$-fold for the MGS-catalyzed elimination. With TIM, where enolization is partially rate limiting, the larger k_{cat} of 800 s^{-1} for isomerization, and the greater catalytic power of 10^9 (*56*), support the view that the lower k_{cat} value of MGS is limited by a step other than enolization, such as the elimination step or the release of phosphate. This point is reinforced by the absence of a primary deuterium kinetic isotope effect in the removal of the *pro-S* proton from DHAP in the MGS-catalyzed reaction (*9*). The fact that the phosphate-leaving group in MGS is surrounded by nine hydrogen bonds that promote its capacity as a leaving group could contribute to a slower product release rate, while fewer hydrogen bonds from TIM to the phosphate permit rapid dissociation.

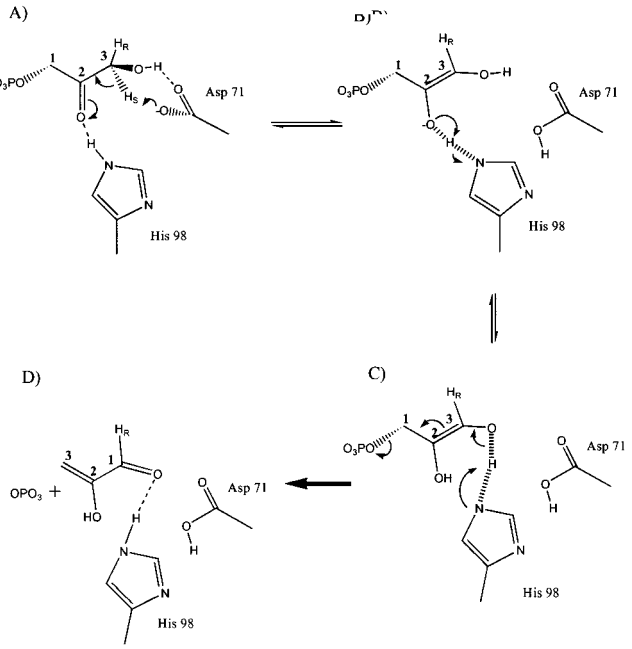

FIGURE 12: Mechanism for MGS based on the mechanism of the TIM reaction (*27*, *28*, *56*−*58*). (A) Asp-71 abstracts the *pro-S* proton, while His-98 stabilizes the enediolate. (B) His-98 protonates the enediolate oxygen via an SSHB. (C) His-98 deprotonates the enediol via a second SSHB. (D) The bound enol of methylglyoxal is shown, which dissociates and ketonizes in solution.

Given these similarities and in the absence of additional data, a reasonable mechanism for the catalytic conversion of DHAP to the enol of methylglyoxal and phosphate by MGS would be to invoke the mechanism currently accepted for TIM. In such a mechanism (Figure 12), Asp-71 (like Glu-165 in TIM) abstracts a proton from C3 of DHAP to form an enediolate that is stabilized by an SSHB between O2 and His-98 [like His-95 in TIM (Figure 12B)]. Because the pK_a of an enediol and of a neutral histidine are matched, this SSHB would provide the energy for enolization. In the second step, His-98 protonates O2 and swings out of the enediolic plane toward O3 to abstract the proton from the O3 hydroxyl (via an SSHB) from the *re* face of the intermediate to initiate elimination of the phosphate, forming the enol of methylglyoxal (Figure 12C,D). The advantages of this mechanism are its simplicity and the fact that it permits proton transfer between groups with similar pK_a's.

However, in the structures of both the MGS and TIM complexes with PGH, an SSHB is observed from the hydroxyl of the PGH to the carboxylate in the active site. It is possible that this SSHB is simply due to the difference in the pK_a of O2 between the enediol intermediate and the inhibitor, and has little to do with the authentic mechanism. Indeed, with TIM there is no obvious mechanistic role for the SSHB from the NOH of PGH to the carboxylate of Glu-165, other than binding the inhibitor (and the intermediate) (*57*). On TIM, PGH also receives an SSHB from His-95 NϵH to its C2−O$^-$ ($\phi = 0.71$, a distance of 2.62 Å) (*3*, *27*), while on MGS a normal hydrogen bond is found between His-98 NϵH and the C2 O$^-$ of PGH. The SSHB from His-95 NϵH to the C2 O$^-$ of PGH found in TIM suggests that PGH properly imitates this aspect of the enediolic intermediate. Further, the difference in this hydrogen bond in TIM and MGS suggests an inherent difference in the mechanisms of these two enzymes. The shorter and stronger hydrogen bond

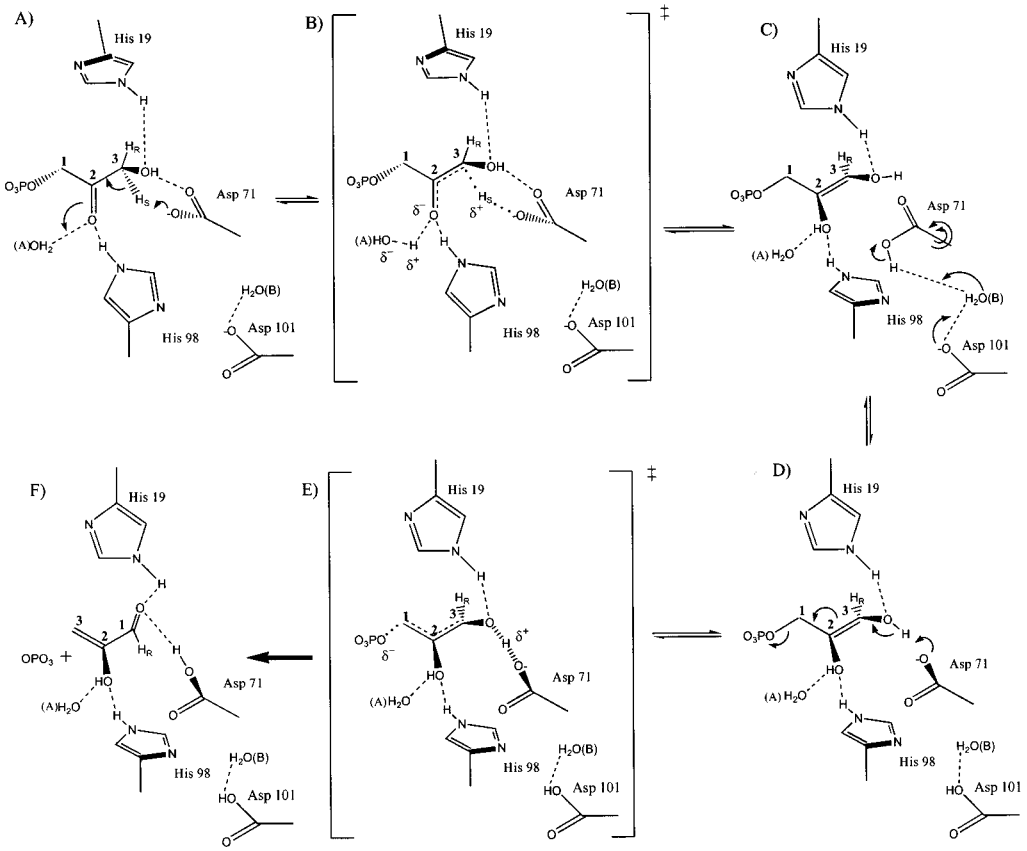

FIGURE 13: Mechanism for MGS based on the structure and affinity of the MGS−PGH complex utilizing an SSHB from Asp-71 to O3 of the *cis*-enediolic intermediate. (A) From the perspective of looking down the plane of the imidazole ring of His-19. The active site of MGS binds a molecule of DHAP. Asp-71 abstracts the *pro-S* carbon-bound proton, and the enolization reaction occurs. (B) The first transition state that forms the enediolic intermediate. (C) Now from the perspective of looking down the imidazole ring of His-98 with the O2 and O3 atoms coming out of the plane of the paper and the bridging oxygen in the plane of the paper. Asp-71 rotates (double curly arrows around the χ_2 bond) to lose its proton to Asp-101 via structural water molecule B. (D) Asp-71 abstracts the enol oxygen proton via an SSHB, and the elimination reaction occurs. (E) The transition state in the elimination of phosphate from the enediolic intermediate. (F) The products enol aldehyde and inorganic phosphate prior to their release from the active site. The enol aldehyde ketonizes to methylglyoxal in solution.

from the NOH of PGH to the carboxylate of Asp-71 in MGS may be mimicking the transition state of the elimination step in the reaction, as proposed in the alternative mechanism of Figure 13. However, the mechanism of Figure 13 is based upon the structure and affinity of the MGS−PGH complex, a ligand with pK_a values different from those of the actual enediolic intermediate. This mechanism is supported in part by the facts that in MGS there is a water molecule (B) buried deep in the active site not found in TIM, the mutation of Asp-101 to Asn leads to a $10^{3.7}$-fold loss in activity, the affinity of PGH for MGS is $10^{2.2}$-fold greater than it is for TIM (*58*), and the affinity is $\sim 10^2$-fold greater than that of PGA for either MGS or TIM. While neither mechanism can be ruled out, the proposed mechanism of Figure 13 accommodates these facts, while the TIM-like mechanism of Figure 12 does not.

In the mechanism of Figure 13, the initial enolization of DHAP (Figure 13A−C) is followed by the abstraction of the enol proton to eliminate phosphate (Figure 13D−F). In the first step, DHAP binds to the enzyme with its hydroxyl O3 accepting a hydrogen bond from His-19 that is out of the plane that is formed by the C2−O2 ketone moiety (Figure 13A). This binding mode, suggested by the conformation of formate found in the MGS−formate/phosphate complex (*22*), positions the C3 *pro-S* proton for abstraction by Asp-71. The pK_a of Asp-71 could be increased to approach that of the C3 proton by the generally hydrophobic environment and by the presence of the negative charge on Asp-101 that is 5.4 Å away, while the pK_a of the C3 proton could be lowered by polarization of the substrate carbonyl group by neutral His-98. The low pK_a of His-98 on MGS is reminiscent of the low pK_a of His-95 on TIM, which has been ascribed to its location at the amino terminus of a short α-helix (*27*). A similar effect may be operative in MGS where the ring nitrogens of His-98 are positioned between the amino termini of helices C and D, which are both approximately 7 Å away. Local hydrophobicity at the active sites of both enzymes may also contribute to the low pK_a's. However, the proximity of Asp-71 to His-98 on MGS and of Glu-165 to His-95 on TIM makes these low pK_a's somewhat surprising.

The resultant negative charge forming on O2 of the incipient enediolate could be stabilized throughout the elimination reaction by hydrogen bonds from His-98 (2.8 Å) and from a bound water molecule, H_2O(A) (2.8 Å). If so, the elimination part of the reaction would need to operate with a negative charge on O2. Alternatively, the negative charge on O2 of the intermediate may be dispersed into the water network by abstracting the proton from water A (as indicated in Figure 13C). Next, Asp-71 loses its proton to Asp-101 through water molecule H_2O(B) that is hydrogen

bonded to the carboxylate of Asp-101 and to the carbonyl oxygen of Gly-66. The removal of this proton from Asp-71 requires the χ_1 and χ_2 torsion angles of this residue to rotate ~10° and ~90°, respectively, to interact with this water that is initially located 4.7 Å away (Figure 13C). The participation of Asp-101 as a proton scavenger is consistent with the kinetics of the D101N mutant enzyme, where k_{cat} is decreased by $10^{3.7}$-fold compared to that of the wild-type enzyme (*2*).

After losing its proton, the negatively charged carboxylate of Asp-71 approaches the 3-OH on the *re* face of the enediolic plane, forming a short (~2.5 Å), strong hydrogen bond, while the "leaving" phosphate group is tilted out of the enediolic plane from the same *re* face (Figure 11). On MGS, Asp-71 and the phosphate are thus positioned to function as the base and leaving group, respectively, in a concerted suprafacial 1,4-elimination of phosphate (Figure 13D−F) as would be predicted by applying the Woodward−Hoffmann rules. According to the Woodward−Hoffmann rules, concerted elimination is forbidden if the leaving group is in the plane of the central sp^2 carbon atom, since a concerted mechanism must follow the principles of "backside" attack (Figure 13D). Note that in TIM, the phosphate is just out of the enediolic plane and on the opposite side relative to the carboxylate of Glu-165. On MGS, the elimination of the leaving phosphate is further facilitated by some of the nine hydrogen bonds donated by seven residues (Figure 4), to yield the enol of methylglyoxal, which dissociates and ketonizes in solution (*9*). Once the products have left the active site, both Asp-71 and Asp-101 need to be deprotonated to return to their initial states.

Neutral His-19, protonated on Nϵ, also approaches the NOH of bound PGH, but on the *si* face. This geometry of His-19 and its potential as a hydrogen bond donor argue against its possible role as the general base in the elimination step (Figure 13D−F). While the true enediolic intermediate may have pK_a's differing from those of PGH at O2 and O3, the relative orientations of His-19 and Asp-71 would not be expected to differ, thus precluding a concerted elimination reaction in step 2 of the MGS reaction if His-19 were the catalytic base.

The inhibition by PGH can be readily understood in terms of the mechanism of Figure 13. With MGS, at pH 7.0, PGH is a tight-binding competitive inhibitor with a K_i of 39 nM. By contrast, with TIM, PGH is a 175-fold weaker competitive inhibitor with a K_i of 7 μM at pH 7.6 (*58*). This inhibition constant is of the same order of magnitude as MGS−PGA and TIM−PGA inhibition constants [2.0 and 4.0 μM, respectively (*2, 24*)] or the MGS−PGH dissociation constant of the D71N mutant enzyme (3.9 μM). In the context of TIM, PGH is thought to be the analogue of the enediol intermediate. However, in the context of MGS, the additional ~3 kcal/mol of binding energy for PGH suggests that this inhibitor is an analogue of the second transition state, in the step from the enediol intermediate to the elimination of phosphate (Figure 13E). Thus, the 2 order of magnitude greater affinity of PGH for MGS compared to that for TIM likely results from the fact that PGH better resembles the second transition state of the MGS mechanism than it does the enediol intermediate of the TIM mechanism. This greater affinity may well result from the shorter, stronger hydrogen bond from PGH NOH to Asp-71 and is not due to the large number of hydrogen bonds to the phosphate, since the inhibition constants of PGA for both enzymes are nearly identical (*2*). However, these hydrogen bonds to the phosphoryl moiety in MGS are likely to enhance the rate of the elimination step, but may slow the rate of product release by stabilizing the bound phosphate.

The likely role for the SSHB from Asp-71 to O3 of the enediolic intermediate is to facilitate transfer of a proton from O3 to the carboxylate of Asp-71, in the second transition state (Figure 13E). While the precise strength of transition state stabilization by this hydrogen bond is unknown, the decreased k_{cat} in the D71N mutant enzyme corresponds to the introduction of a barrier to catalysis of *at least* 4.7 kcal/mol.[3] However, interpreting the effects of the D71N mutation is difficult since Asp-71 is now thought to abstract both the *pro-S* C3 proton (Figure 13A−C) as well as the enol oxygen (O3) proton (Figure 13D−F). Since the decrease in the K_i for the transition state inhibitor PGH is only $10^{2.2}$-fold, a simple interpretation is that PGH is not a perfect analogue and thus PGH binding is not stabilized as much by MGS as is the actual transition state. An alternative interpretation is that the barrier to catalysis represented by the second transition state (Figure 13D) is not as large as that represented by the first transition state (Figure 13B), since a covalent carbon−hydrogen bond is stronger than an oxygen−hydrogen bond. The fact that no primary deuterium kinetic isotope was detected for the removal of the *pro-S* proton from DHAP (*9*) indicates that enediol(ate) formation is probably not rate-limiting in the enzymatic reaction, despite the observation that enediol(ate) formation is largely rate-limiting in the nonenzymatic, hydroxide-catalyzed reaction (*54*, *55*). If the barrier to catalysis represented by the first transition state is indeed higher than the second transition state, a conformation change or product release must be the overall rate-limiting step for MGS catalysis. As suggested by the structure (Figure 3) and by phosphate inhibition (*2*, *59*), the release of phosphate is more likely to be rate-limiting than the release of the enol or enolate of methylglyoxal.

CONCLUSIONS

Two reasonable mechanisms for MGS have been considered (Figures 12 and 13). In the TIM-like mechanism of Figure 12, Asp-71 abstracts the C3 proton of DHAP, while the role of His-98 is to protonate O2 of the enediolate intermediate and subsequently to deprotonate O3 of the enediol intermediate in the elimination of phosphate. While the mechanism of Figure 12 cannot be excluded, the alternative mechanism of Figure 13 suggested by X-ray crystallographic, NMR spectroscopic, and binding studies of the MGS−PGH complex proposes that Asp-71 not only acts to abstract the carbon-bound proton by analogy with TIM in step 1, but also abstracts the proton from the enol O3 of the enediolic intermediate in step 2. Specifically, the SSHB found between the carboxylate of Asp-71 and the NOH of the hydroxamic acid is analogous to that proposed to form in the second transition state. In the mechanism of Figure 13, neutral His-98 likely polarizes the C2 carbonyl group of the substrate to maintain the C2═C3 double bond. However, the current structural and spectroscopic data do not provide information about the charge on O2 of the intermediate.

ACKNOWLEDGMENT

We thank Dr. June Messmore for useful discussions and technical advice. We also thank Dr. Darrell R. McCaslin for rapid access to the ITC instrument at the Biophysics Instrumentation Facility at the University of Wisconsin (Madison, WI), which was established by Grant BIR-9512577 (NSF).

REFERENCES

1. Schowen, K. B., and Schowen, R. L. (1982) *Methods Enzymol. 87*, 551−606.
2. Saadat, D., and Harrison, D. H. T. (1998) *Biochemistry 37*, 10074−10086.
3. Harris, T. K., and Mildvan, A. S. (1999) *Proteins 35*, 275−282.
4. Lipscomb, W. N. (1980) in *Methods for Determining Metal Ion Environments in Proteins* (Darnall, D. W., and Wilkins, R. G., Eds.) Elsevier, New York.
5. Mildvan, A. S., Harris, T. K., and Abeygunawardana, C. (1999) *Methods Enzymol. 308*, 219−245.
6. Wei, Y., and McDermott, A. (1999) in *Modeling NMR Chemical Shifts: Gaining Insight into Structure and Environment. Methods of Enzymology*. (Facelli, J. C., and deDios, A. C., Eds.) pp 177−193, Oxford University Press.
7. Viragh, C., Harris, T. K., Reddy, P. M., Massiah, M. A., Mildvan, A. S., and Kovach, I. M. (2000) *Biochemistry 39*, 16200−16205.
8. Kuhn, P., Knapp, M., Soltis, S. M., Ganshaw, G., Thoene, M., and Bott, R. (1998) *Biochemistry 37*, 13446−13452.
9. Summers, M. C., and Rose, I. A. (1977) *J. Am. Chem. Soc. 99*, 4475−4478.
10. Albery, W. J., and Knowles, J. R. (1976) *Biochemistry 15*, 5631−5640.
11. Cooper, R. A., and Anderson, A. (1970) *FEBS Lett. 11*, 273−276.
12. Cooper, R. A. (1984) *Annu. Rev. Microbiol. 44*, 812−826.
13. Rahman, A., Shahabuddin, M., and Hadi, S. M. (1990) *J. Biochem. Toxicol. 5*, 161−166.
14. Papoulis, A., al-Abed, Y., and Bucala, R. (1995) *Biochemistry 34*, 648−655.
15. Baskaran, S., and Balasubramanian, K. A. (1990) *Biochem. Int. 21*, 165−174.
16. Együd, L. G., and Szent-Györgyi, A. (1966) *Proc. Natl. Acad. Sci. U.S.A. 56*, 203−207.
17. Clelland, J. D., and Thornalley, P. J. (1993) *Biochem. Soc. Trans. 21*, 160S.
18. Tötemeyer, S., Booth, N. A., Nichols, W. W., Dunbar, B., and Booth, I. R. (1998) *Mol. Microbiol. 27*, 553−562.
19. Brownlee, M., and Cerami, A. (1981) *Annu. Rev. Biochem. 50*, 385−432.
20. Murthy, N. S., Bakeris, T., Kavarana, M. J., Hamilton, D. S., Lan, Y., and Creighton, D. J. (1994) *J. Med. Chem. 37*, 2161−2166.
21. Cameron, D. C., Altaras, N. E., Hoffman, M. L., and Shaw, A. J. (1998) *Biotechnol. Prog. 14*, 116−125.
22. Saadat, D., and Harrison, D. H. T. (1999) *Struct. Folding Des. 7*, 309−317.
23. Saadat, D., and Harrison, D. H. T. (2000) *Biochemistry 39*, 2950−2960.
24. Lolis, E., and Petsko, G. A. (1990) *Biochemistry 29*, 6619−6625.
25. Collins, K. D. (1974) *J. Biol. Chem. 249*, 136−142.
26. Davenport, R. C., Bash, P. A., Seaton, B. A., Karplus, M., Petsko, G. A., and Ringe, D. (1991) *Biochemistry 30*, 5821−5826.
27. Lodi, P. J., and Knowles, J. R. (1991) *Biochemistry 30*, 6948−6956.
28. Harris, T. K., Abeygunawardana, C., and Mildvan, A. S. (1997) *Biochemistry 36*, 14661−14675.
29. Harris, T. K., Marks, G. T., Massiah, M. A., Mildvan, A. S., and Harrison, D. H. T. (2000) 220th National Meeting of the American Chemical Society, Aug 20−24, Washington, DC, Abstract 507.
30. Laemmli, U. K. (1970) *Nature 227*, 680−685.
31. Turner, D. L. (1983) *J. Magn. Reson. 54*, 146−148.
32. Marion, D., Ikura, M., Tschudin, R., and Bax, A. (1989) *J. Magn. Reson. 85*, 393−399.
33. Levy, G. C., and Lichter, R. L. (1979) in *Nitrogen-15 Nuclear Magnetic Resonance Spectroscopy*, John Wiley & Sons, New York.
34. Sklenar, V., and Bax, A. (1987) *J. Magn. Reson. 74*, 469−479.
35. Smallcomb, S. H. (1993) *J. Am. Chem. Soc. 115*, 4776−4785.
36. Hopper, D. J., and Cooper, R. A. (1972) *Biochem. J. 128*, 321−329.
37. Kuzmic, P., Sideris, S., Cregar, L. M., Elrod, K. C., Rice, K. D., and Janc, J. W. (2000) *Anal. Biochem. 281*, 62−67.
38. Segel, I. H. (1975) in *Enzyme Kinetics: Behavior and Analysis of Rapid Equilibrium and Steady-State Enzyme Systems*, pp 346−462, John Wiley & Sons, New York.
39. Wiseman, T., Williston, S., Brandts, J. F., and Lin, L.-N. (1989) *Anal. Biochem. 179*, 131−137.
40. Okamoto, K., Hara, S., Bhasin, R., and Freundlich, M. (1988) *J. Bacteriol. 170*, 5076−5079.
41. Otwinowski, Z., and Minor, W. (1996) in *Modeling NMR Chemical Shifts: Gaining Insight into Structure and Environment. Methods of Enzymology.* (Carter, C., and Sweet, R. M., Eds.) pp 307−325, Academic Press, Boston.
42. Brünger, A. T. (1992) *Nature 355*, 472−474.
43. Kleywegt, G. J., and Jones, T. A. (1996) *Acta Crystallogr. D52*, 826−828.
44. Kleywegt, G. J., and Jones, T. A. (1995) *Structure 3*, 535−540.
45. Brünger, A. T. (1992) *X-PLOR, Version 3.1, A system for X-ray crystallography and NMR*, Yale University Press, New Haven, CT.
46. Jones, T. A., Zou, J. Y., Cowan, S. W., and Kjeldgaard, M. (1991) *Acta Crystallogr. A47*, 110−119.
47. Williams, J. W., and Morrison, J. F. (1979) *Methods Enzymol. 63*, 437−467.
48. McDermott, A., and Ridenour, C. F. (1996) in *Encyclopedia of NMR*, pp 3820−3825, John Wiley & Sons, Sussex, U.K.
49. Kreevoy, M. M., and Liang, T. M. (1980) *J. Am. Chem. Soc. 102*, 3315−3322.
50. Hibbert, F., and Emsley, J. (1990) *Adv. Phys. Org. Chem. 26*, 255−379.
51. Arrowsmith, C. H., Guo, H.-X., and Kresge, A. J. (1994) *J. Am. Chem. Soc. 116*, 8890−8894.
52. Guo, H.-X., and Kresge, A. J. (1997) *J. Chem. Soc., Perkin Trans. 2*, 295−298.
53. Brill, V. R., and Tippe, A. (1967) *Acta Crystallogr. 23*, 343−345.
54. Richard, J. P. (1984) *J. Am. Chem. Soc. 106*, 4926−4936.
55. Richard, J. P. (1993) *Biochem. Soc. Trans. 21*, 549−553.
56. Nickbarg, E. B., and Knowles, J. R. (1988) *Biochemistry 27*, 5939−5947.
57. Harris, T. K., Cole, R. N., Comer, F. I., and Mildvan, A. S. (1998) *Biochemistry 37*, 16828−16838.
58. Zhang, Z., Komives, E. A., Sugio, S., Blacklow, S. C., Narayana, N., Xuong, N. H., Stock, A. M., Petsko, G. A., and Ringe, D. (1999) *Biochemistry 38*, 4389−4397.
59. Hopper, D. J., and Cooper, R. A. (1971) *FEBS Lett. 13*, 213−216.
60. Laskowski, R. A., MacArthur, M. W., Moss, D. S., and Thornton, J. M. (1993) *J. Appl. Crystallogr. 26*, 548−558.
61. Engh, R. A., and Huber, R. (1998) *Acta Crystallogr. A47*, 392−400.

BI0028237